One-step electrodeposition of Pd-CeO2 on high pore density foams for environmental catalytic processes

Catalysis Science & Technology

ARTICLE

One-step electrodeposition of Pd-CeO_2 on high pore density foams for environmental catalytic processes

Received 00th January 20xx,
Accepted 00th January 20xx

DOI: 10.1039/x0xx00000x

www.rsc.org/

P. H. Ho[a,b], M. Ambrosetti[c], G. Groppi[c,**], E. Tronconi[c], J. Jaroszewicz[d], F. Ospitali[a], E. Rodríguez-Castellón[e], G. Fornasari[a], A. Vaccari[a], P. Benito[a,*]

Environmental catalytic processes are probably the best example for the application of structured catalysts based on activated open-cell metallic foams, and Pd on CeO_2 is one of the most active catalysts for different applications like three way catalysts, methane combustion and water gas shift. Here, we report the one-step deposition of Pd and CeO_2 on FeCrAlloy foams with very high pore densities (cell size equal to 580 and 1200 µm) by the electro-base generation method followed by calcination. The type of Pd and CeO_2 species, the quality of the coating and the catalytic activity in the mass transfer limited CO oxidation as a model reaction were investigated. For comparison purposes, a CeO_2 coating was also prepared. Reproducible and evenly distributed defective nano-CeO_2 coatings containing $Pd_xCe_{1-x}O_{2-\delta}$ solid solution and Pd^0 particles were electrodeposited in 500 s regardless of the foam pore size. The structure, morphology, and adhesion of the catalytic layer, as well as the Pd distribution, were almost constant after calcination at 550 °C, only some PdO segregated. The resulting structured catalysts showed high activity and stability after 48 h time-on-stream and different thermal cycles in CO oxidation even at high GHSV values (e.g. $4x10^6$ h^{-1} referred to the total foam disk volume). High volumetric mass transfer coefficients, widely outperforming those of conventional honeycomb monoliths, were obtained, especially for the small pore (580 µm) foam. The *in situ* formation of Pd^0 nanoparticles and the homogeneous distribution and stability of the coating may contribute to the high catalytic performance, although these catalyst features depended on the position in the catalytic bed.

Introduction

Pd/CeO_2 based catalysts on honeycomb monoliths are constitute the three-way catalysts (TWC).[1] These so-called structured catalysts merge the activity of the coating with the low pressure drop and enhanced mass and heat transfer of the support. Alternatives to the conventional honeycomb supports are metallic open-cell foams[2] and fibers,[3] made for instance of FeCrAlloy. In particular, open-cell metallic foams are getting increasing interest as 3D supports since they are light-weight, have a high specific mechanical strength, and large geometric surface area; moreover, their open cellular structure provides a disruptive and tortuous flow path and hence an exceptional mixing as well as supply or release of the heat to/from the surface.[4] Moreover, these structured catalysts could find application in processes where the activity of Pd/CeO_2 has been demonstrated, such as methane combustion[5-8] and water gas shift.[9-11] In these applications, Pd/CeO_2 coated metallic foams have been reported to provide a unique combination of high low-temperature activity/selectivity, good catalyst stability and low conversion oscillations, low pressure drop at high-throughput operation, and enhanced heat transfer. Moreover, in methane combustion they allow for low Pd usage,[12] while in Water Gas Shift the redistribution of the heat over the bed allows to increase the CO conversion and the reaction rate.[13]

The properties of the structured catalysts based on metallic foams are related to geometric parameters, i.e. pore and strut diameter and void fraction, which can be tailored by foam producers. They not only determine the geometrical surface area for coating but also the pressure drop and gas-solid mass and heat transfer coefficients[14, 15] as well as the effective thermal conductivity.[16] The smaller the pores, the larger the surface area available to coat the catalytic layer and the better the mass and heat transfer; however, a balance between pore size and pressure drop should be considered.

Conventional washcoating is usually carried out to deposit catalytic layers on medium and large pore open-cell foam supports, i.e. 20, 40, 60 pores per inch (ppi).[17-19] Few works deal with the coating of small pore size foams,[20] probably related to pore blockage and inhomogeneous coating distribution. Other techniques, such as galvanic displacement[21] and hydrothermal synthesis followed by incipient wetness impregnation of the active phase[22] have been proposed to coat foams up to 100 ppi. The

[a] Dipartimento di Chimica Industriale "Toso Montanari", Università di Bologna, Viale Risorgimento 4, 40136, Bologna, Italy.
[b] Institut für Technische und Makromolekulare Chemie, RWTH Aachen University, Worringerweg 2, 52074 Aachen, Germany.
[c] Laboratory of Catalysis and Catalytic Processes, Dipartimento di Energia, Politecnico di Milano, Via La Masa 34, 20156, Milano, Italy.
[d] Faculty of Materials Science and Engineering, Warsaw University of Technology, 141 Woloska Str., 02-507 Warsaw, Poland.
[e] Departamento de Química Inorgánica, Facultad de Ciencias, Universidad de Málaga, 29071 Málaga, Spain.
* Email: patricia.benito3@unibo.it.
** Email: gianpiero.groppi@polimi.it
Electronic Supplementary Information (ESI) available: [details of any supplementary information available should be included here]. See DOI: 10.1039/x0xx00000x

former allows to deposit Pd directly onto the foam, but without co-deposition of oxide layer. In the latter, it is possible to integrate simultaneously an oxide or its precursor on the foam by a direct synthesis but the precipitation may also occur in the bulk of the solution, with the consequent loss in efficiency.

The electro-base generation method is suitable to coat 60-80 ppi metallic foams with hydroxides such as hydrotalcite-type compounds to obtain structured catalysts after thermal treatment.[23, 24] CeO_2 can be also easily synthesized by this method, although most of the published works report the coating of simple shaped supports such as foils (Ni), sheets (stainless steel), and disks (Pt, Au, platinized silicon wafer, stainless steel).[25-28] Coatings with tailored morphology (flaky,[28, 29] compact particles,[28] nanocubes and nanowires[30]) and thickness (from nanostructured films[26, 29] to 30 µm[27]) can be obtained on steel, whose main applications are the suppression of corrosion processes and in fuel cells. The deposition involves the electro-generation of a base in the electrode/electrolyte interface; when the pH suitable for the Ce^{3+} precipitation is attained, $Ce(OH)_3$ is firstly obtained, then Ce^{3+} is oxidized, the hydroxide dehydrated and subsequently transformed into CeO_2.[27] This is rather easily achieved in short times after application of a constant cathodic potential or current to the working electrode dipped in either a $Ce(NO_3)_3$ or $CeCl_3$ solution saturated with O_2 or air.[26, 29]

The electrodeposition is more challenging when performed on complex shaped supports and in presence of a highly reducible cation in the electrolytic solution, such as the case of the electrodeposition of Pd-CeO_2 catalysts on metallic foams. To achieve a highly active structured catalyst, for instance in the mass transfer limited CO oxidation, the coating thickness, distribution and adhesion to the metallic support are of paramount importance,[31] but also the Pd oxidation state,[32, 33] particle size[33-35] and interaction with the CeO_2 (forming a $Pd_xCe_{1-x}O_{2-\delta}$ solid solution).[36, 37] Catalysts with such tailored properties are prepared by coprecipitation with a base,[35, 38-41] namely by the same process that should occur during the electro-base generation method. However, the electrodeposition conditions may provoke the uncontrolled deposition of large metallic particles and thin coatings, such as recently reported during the electrodeposition of Pt-CeO_2 on FeCrAlloy foams.[42]

The aim of this work was to electrodeposit in one-step Pd-CeO_2 for the first time on high or medium density cell FeCrAlloy foams (with a nominal cell diameter equal to 580 and 1200 µm, which according to visual inspection of foam micrographs roughly correspond to 100 and 60 ppi, respectively). After calcination at 550 °C, the activity of the samples was evaluated in the mass transfer limited CO oxidation, as a model reaction. The samples were fully characterized after electrodeposition, calcination and catalytic tests to investigate the type of Pd and CeO_2 and the quality and adhesion of the coating. For comparison purposes on the coating properties, a foam was also coated with only CeO_2.

Experimental

Catalysts preparation

9 mm disks of FeCrAlloy open-cell foams with a nominal cell size equal to 580 and 1200 µm and thickness of 1.9 and 3.1 mm, respectively were cut from commercial panels from Alantum GmbH and used as structured supports. Prior to use, the foams were washed in acetone, water and then dried at 40 °C for 24 h.

The electrolyte was an aqueous solution of $PdCl_2$ (> 99%, Sigma-Aldrich) and $Ce(NO_3)_3$ (> 98%, Sigma-Aldrich), 0.15 M total concentration, and atomic ratio (a.r.) Pd/Ce = 3/97 to give a Pd nominal loading of 2 wt.% in the final catalyst. A given amount of $PdCl_2$, calculated for 250 mL electrolyte, was firstly dissolved in 10 mL of distilled water with the addition of 0.1 g concentrated of HCl (37%) and kept under stirring and heating at 50 °C. When the solution became transparent orange colour, the rest of water and $Ce(NO_3)_3$ were added to obtain the electrolyte. The final pH of the solution before the synthesis was approximately 2.5–2.7. For comparison purposes, samples containing only CeO_2 were synthesized from a 0.15 M $Ce(NO_3)_3$ electrolyte.

Electrodepositions were performed in a homemade double-compartment flow electrochemical cell by FAVS Gnudi, using a potentiostat (Autolab, PGSTAT128N, Eco Chemie) with GPES software. A Pt coil (0.4 mm diameter and 40 cm in length) and a saturated calomel electrode (SCE) were used as counter and reference electrode (C.E. and R.E.), respectively. The working electrode (W.E.) was the FeCrAlloy foam disk and it was assembled by a two-pronged Pt electrical contact. The working and counter electrode compartments were separated by a glass frit tube to avoid the mixture of the electrochemical reaction products. The R.E. was in electrolytic contact with the main compartment *via* a Luggin capillary placed 1 mm close to the surface of the foam cylinder. All potentials were reported with respect to SCE. The electrodepositions were performed at -1.2 V *vs* SCE for 500 s with circulation of the electrolyte at a flow rate of 2 mL min^{-1} as described elsewhere.[43] It should be noted that in these electrolytes, the set-up reached a low uncompensated resistance (R_u) ca. 1-2 Ω in all of experiments. After electrodeposition, the coated foams were thoroughly washed with distilled water and dried at 120 °C for 24 h. The samples were then calcined at 550 °C for 10 h with a heating rate of 10 °C min^{-1}.

Characterization techniques

Scanning electron microscopy (SEM) coupled with energy dispersive spectrometry (EDS) was performed by using an EP EVO 50 Series Instrument (EVO ZEISS) equipped with an INCA X-act Penta FET® Precision EDS microanalysis and INCA Microanalysis Suite Software (Oxford Instruments Analytical) to provide images of the spatial variation of elements in a sample. The accelerating voltage was 20 kV and the spectra were collected for 60 s. As-prepared, calcined and spent coated foams were analysed in 3–4 regions of interest. The average Pd/Ce a.r. ratio values were estimated for 5 different foams. The thickness of the coated layers was estimated from images where the solid developed cracks.

During SEM/EDS analysis, Micro-Raman spectra were *in situ* recorded by a Renishaw Raman SCA (*Structural and Chemical Analyser for SEM*) probe linked by optical fiber to a Renishaw Raman Invia spectrometer. The electron and laser beam (Ar^+ laser source λ = 514.5 nm, P_{out} = 30 mW considering the decrease in power due to the plasma filter) are confocal. By this way, it was possible to analyse different locations of the where the compositions were identified by EDS. In each measurement, the laser power was set by 10% of the source and the signal was accumulated by four individual spectra with a 30 s acquisition time.

Field emission scanning electron microscopy (FE-SEM) analyses were conducted on a Zeiss LEO Gemini 1530 equipped with an Everhart-Thornley (E-T) secondary electron detector and a

Scintillator BSE detector – KE Developments CENTAURUS. The accelerating voltages were 5 or 10 kV.

Disk samples (before and after electrodeposition) were scanned using a microfocussed X-ray tomographic system (MICRO XCT-400 Xradia, Zeiss), at 80 kV and 125 µA. For each sample, 1500 projection images were recorded with an exposure time of 22 sec. The volume was reconstructed with the instrument software and was then exported to CTAn (SkyScan, Bruker) for further 3D image analysis. Voxel size was the same for all samples (5×5×5 µm). Porosity was calculated by simple voxel counting in the 3D binary image after segmentation; the error in the measurements below is 0.1%, derived from image processing and scan resolution. Thickness of the struts and nodes, named solid structure thickness, was calculated using a model independent sphere filling technique,[44] it corresponds to the mean diameter of the spheres that could fill the solid structure. The mean pore size is the average pore volume of equivalent sphere diameter. To obtain direct comparison, the CT scans were performed firstly on the bare foam and then on the same locations of this foam but after being coated with Pd-CeO_2 by the electrodeposition. The image registration process was achieved using the DataViewer 3D Registration Tool (SkyScan, Bruker).

The X-ray diffraction (XRD) analysis of the film grown on the foam was carried out using a PANalytical X'Pert diffractometer equipped with a copper anode (λ_{mean} = 0.15418 nm) and a fast X'Celerator detector. Wide-angle diffractograms were collected over 2θ range from 20 to 70° with a step size of 0.07° and counting time 600 s. The cell parameters of the detected phases could not be obtained since the surface of the analysed samples was not planar. Small modifications in the reflection positions could be related to differences in the radiation paths rather than the incorporation of Pd^{2+} into the CeO_2 lattice.

Chemical composition of the Pd-CeO_2 coatings was analysed by ICP-OES measurements using an instrument ICP Thermo Elemental IRIS Intrepid (Thermo Scientific). The foam catalysts were mineralized with a mixture of HNO_3/$HClO_4$ and then diluted with UPP-water to obtain suitable concentrations for a sufficient detection of each element. Concentrations of Pd and Ce were obtained by quantification of the peak areas at 324.27 and 413.38 nm, respectively.

N_2 adsorption-desorption isotherms were measured at -196 °C using a Micromeritics ASAP 2020 instrument. Prior each measurement, the coated foams were degassed via two steps: at 150 °C for 30 min under a pressure of 30 µmHg and then 250 °C for 30 min (150 °C for not calcined samples). The specific surface area (S_{BET}) was calculated using the Brunauer-Emmett-Teller (BET) multiple-point method in the relative 0.05 to 0.3 pressure range p/p_o.

High resolution transmission electron microscopy (HRTEM) characterization was carried out by a TEM/STEM FEI TECNAI F20 microscope, equipped with an EDS analyser. Powder catalysts were collected by scratching the foam surface and then suspended in ethanol under ultrasounds for 20 min. The suspension was subsequently deposited on a Cu grid with lacey quanti-foil carbon film and dried at 100 °C before doing the measurement. Selected Area Electron Diffraction (SAED) and Fast Fourier Transformation (FFT) were used to determine the interplanar spacing of the crystals. Particle size distribution was processed considering around 150 particles in three different zones for each sample.

X-Ray photoelectron spectra (XPS) studies were carried on a Physical Electronics spectrometer (PHI Versa Probe II Scanning XPS Microprobe) with monochromatic X-ray Al Kα radiation (100 µm, 100 W, 20 kV, 1,486.6 eV) and a dual beam charge neutralizer. Charge referencing was measured against adventitious carbon (C 1*s* at 284.8 eV). A PHI ACCESS ESCA-V6.0 F software package was used for acquisition and data analysis. A Shirley-type background was subtracted from the signals. Recorded spectra were always fitted using Gaussian–Lorentzian curves in order to determine the binding energies of the different element core levels more accurately.

Temperature programmed reduction by H_2 (H_2-TPR) was performed in an AutoChem II (Chemisorption analyzer, Micromeritics) with one coated foam. The catalyst was firstly outgassed at 150 °C under 30 mL min^{-1} of He for 30 min. After cooling to -10 °C by vapor of liquid N_2, the carrier gas was switched to 5 % H_2/Ar (v/v) at 30 mL min^{-1}. When the baseline was stable, the temperature was increased to 900 °C with a ramp of 10 °C min^{-1}, while the amount of H_2 consumed was measured by means of a thermal conductivity detector (TCD).

Catalytic tests

Evaluation of the catalytic activity of electrodeposited samples was performed running CO catalytic oxidation. This reaction is considered a model reaction for environmental applications and it is usually adopted for the analysis of mass transfer performances since it is active at low temperature and does not produce intermediates.

A schematic view of the reactor used for the catalytic tests is reported in Fig. 1. The samples with a diameter equal to 9 mm were loaded in a pipe with internal diameter of 9 mm and external diameter of 11 mm. This pipe was then inserted in a threaded tubular reactor fixed with a screw and placed in an oven. At the top and at the bottom of the catalytic samples, additional bare foams were added in order to increase the bed length and avoid inlet effects acting as flow distributors: in particular, for 1200 µm foams, other two non-activated samples with same morphological features were used in the inlet and outlet section, while for 580 µm foam the inlet bed was composed by two 1200 µm foams and a single 580 µm foam disk maintaining the same downstream configuration. Two K-type thermocouples were inserted in the reactor to measure the temperature upstream and downstream the catalytic bed (Thermocouple 1 and 2, respectively in Fig. 1). Carbon monoxide and air provided by SAPIO® were fed through stainless steel lines and regulated with BROOKS mass flow controllers; gases were mixed and preheated in a coil up to 175 °C before entering in the reaction zone.

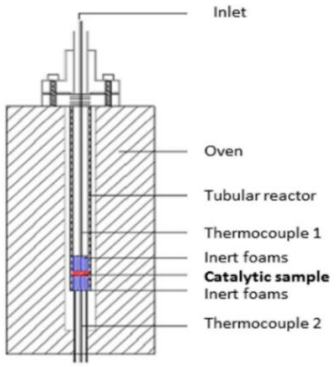

Fig. 1. Layout of the reactor.

Effects of the flow rates on the CO combustion were assessed investigating different flow rates in the range 1000–9000 cm^3 min^{-1} at STP (1 – 9 SLM). In order to observe the effect of CO concentration on light-off curves and on the conversion at diffusive regime, for some of the flow rates, the inlet CO concentration was varied from 2 to 3% (v/v) in air. During each test the oven temperature was increased stepwise in order to change the inlet temperature, after reaching steady state conditions for the temperatures, the conversion of CO was determined by the analysis of the reaction products; the overall errors detected in carbon balances were in the range 1-3%. Only analyses before the proper ignition point or in the plateau regime when the reaction is almost under complete diffusive control were performed, due to the problematic control of the temperature in the kinetically-limited regime. Due to the exothermic character of the reaction, temperature differences up to 120 °C across the foam bed were observed in the achieved mass transfer regime.

Before performing the catalytic tests, blank tests with non-active foams were performed in order to confirm the absence of homogeneous reaction and avoid any effect in the conversion induced by the setup or the bare supports - conversions lower than 4% were observed up to 450 °C.

Tests at low flow rate - 1000 cm^3 min^{-1} at STP (1 SLM) – were performed to exclude any preferential flow path inside the reactor; in these tests, almost complete conversion was observed ensuring adequate activity of the catalyst and allowing to exclude the presence of a significant bypass.

Results and Discussion

Characterization of as-deposited foams

Open-cell foams were easily and quickly coated, regardless of the pore size, by a sole cerium-containing 5 µm film of graded morphology (Fig. 2a-a3). Platelet-like particles with their planes oriented perpendicular to the foam surface (Fig. 2a1, a2), giving rise to a highly porous coating characteristic of electrodeposited CeO_2,[28] and a very compact layer laying on it (Fig. 2a1, a3) precipitated during the cathodic pulse. A graded morphology was previously reported for electrodeposited CeO_2,[45] however, in that case the outer layers showed a needle-like morphology and the inner layers were more compact. Solid loadings of ca. 11-12 wt.% were estimated on both types of foams.

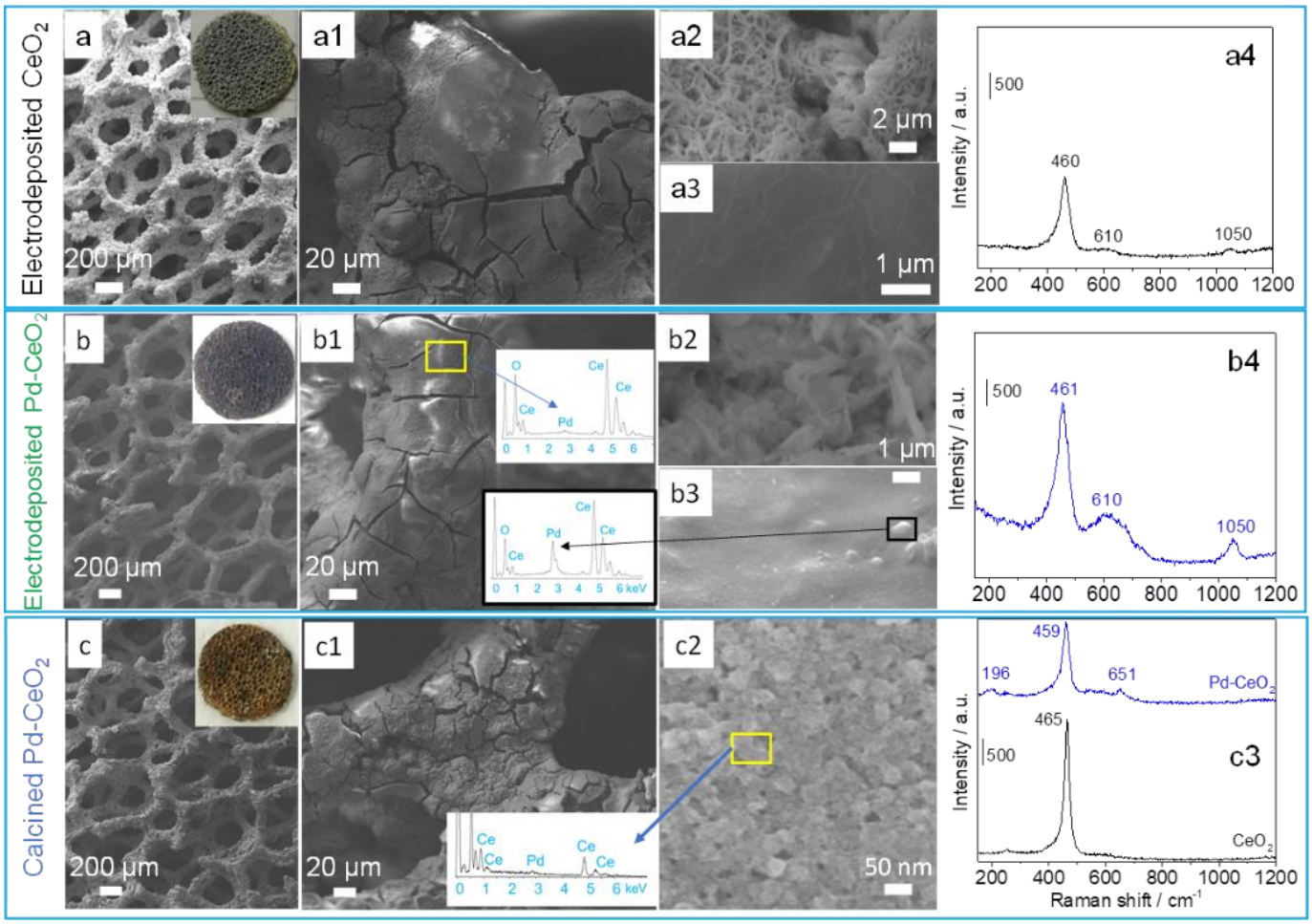

Fig. 2. Characterization of coatings on 580 µm foams. CeO_2: SEM images (a, a1, a2, a3), Raman spectrum (a4); Pd-CeO_2: SEM images, EDS spectra (b, b1, b2, b3), Raman spectrum (b4); calcined Pd-CeO_2: (c, c1, c2) SEM, FESEM images, EDS spectra, (c3) Raman spectra, also CeO_2 calcined.

The structural characterization of the films by XRD confirmed the formation of the cubic fluorite CeO_2 phase (Fig. 3). In the Raman spectra (Fig. 2a4), the coexistence of the F_{2g} mode of CeO_2 at ca. 460 cm^{-1} and a shoulder at ca. 610 cm^{-1} evidenced that the ceria contained structural defects such as oxygen vacancies. The band at ca. 1050 cm^{-1} confirmed the entrapment of nitrates into the CeO_2 structure during the electrodeposition.[46, 47]

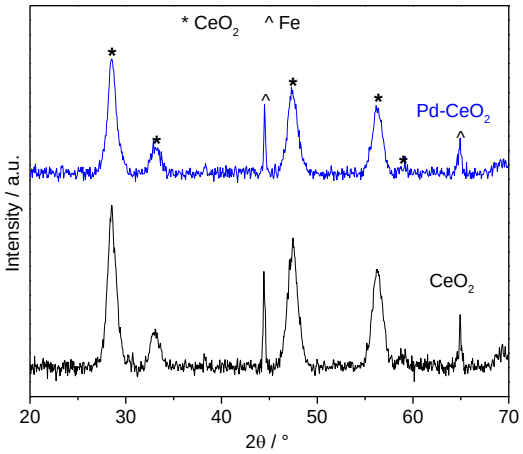

Fig. 3. XRD patterns of CeO_2 and Pd-CeO_2 electrodeposited on 580 µm foams.

Good and reproducible coatings made by porous and compact layers were also achieved with Pd-CeO_2 (Fig. 2b-b3, Fig. S1a-a3), nonetheless a larger amount of material than for CeO_2 deposited, 25.6 ± 1.2 and 22.6 ± 1.3 wt.% for 580 and 1200 µm foams, respectively. Excluding some regions where palladium clusters were clearly identified (Fig. 2b3), Pd-containing species were well dispersed on the coating (Fig. 2b1, 2b2), i.e. Pd signal was detected by EDS but there were no Pd particles observed. Average Pd/Ce a.r. ratio values in these regions were around 3/97, corresponding to the nominal value in the electrolytic solution (2% w/w). However, ICP analysis of the detached coatings gave a 5/95 atomic ratio for both types of foams, i.e. 3 wt.% Pd loading in the electrodeposited catalysts, since it measured Pd well dispersed and present in clusters. The total Pd loading in the structured catalyst considering the foam weight was around 0.54 wt.%. The surface area values for the coated foams were 11.3 and 10.8 $m^2\ g^{-1}$ for 1200 and 580 µm, respectively (Table 1), which normalized to the solid loading corresponded to 52.3 – 40.6 $m^2\ g^{-1}$. The isotherms obtained were characteristics of macroporous or non-porous materials with interparticle pores (Fig. S2).[48]

Table 1. Specific surface area (S_{BET}) values and normalized to the solid loading of the coated 580 µm and 1200 µm foams (fresh and calcined)

Sample	S_{BET} ($m^2\ g^{-1}$)			
	Fresh	Fresh coating	Calcined	Calcined Coating
Pd-CeO_2 – 1200 µm	11.3	52.3	11.1	64.5
Pd-CeO_2 – 580 µm	10.8	40.6	11.9	54.1

XRD patterns showed the reflections of cubic CeO_2 and neither Pd^0 nor PdO phases were identified (Fig. 3). In comparison to the CeO_2 sample, the broadening of the F_{2g} mode and the increase in the defect band intensity in Fig. 2b4 suggested the incorporation of Pd^{2+} in the CeO_2 matrix.[32, 40] The Pd 3*d* core level XPS spectra showed two doublets at binding energies (BE) 335.5-340.7 eV and 337.9-343.2 eV (Fig. 4), confirming the presence of two types of Pd species on the coating surface. The contribution at 335.5 eV was related to Pd^0, while the one at 337.9 eV was attributed to the formation of the $Pd_xCe_{1-x}O_{2-\delta}$ solid solution.[36, 40, 49, 50] The Pd content determined by XPS was 2.49 wt.%. Concerning to Ce 3*d* core level spectra (Fig. S3), in all cases four spin-orbit doublets denoted as *v* and *u* can be observed. Three doublets were ascribed to the presence of Ce^{4+}: *v* (~ 882.3 eV) and *u* (~ 901.0 eV); *v''* (~ 888.7 eV) and *u''* (~ 907.3 eV); *v'''* (~ 898.5 eV), u''' (~ 917.0 eV). Meanwhile, a doublet *v'* (~ 885.3) and *u'* (~ 903.7 eV), assigned to Ce^{3+}, presented a weak intensity due to the low proportion of Ce^{3+}.[51] Both Ce^{4+} and Ce^{3+} were therefore present in the electrodeposited solids, but with a major presence of Ce^{4+}.

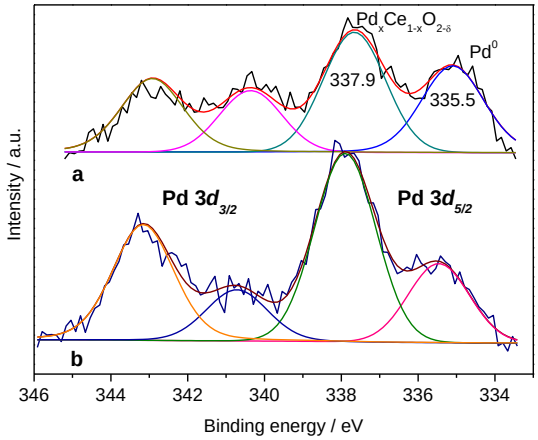

Fig. 4. XPS spectra of Pd core 3d in Pd-CeO_2 coated on 580 µm foams: (a) electrodeposited and (b) calcined sample.

In conclusion, the increase of the pH due to nitrate reduction provoked the easy and homogeneous precipitation of CeO_2 on the foam surface. Moreover, the local pH increase allowed the incorporation of Pd^{2+} into the CeO_2 structure forming the solid solution, as per conventionally coprecipitated samples.[40] The massive deposition of large Pd metallic particles was decreased, but not completely avoided, probably because of the use of palladium chloride precursors.[52] The electrochemical reduction of Pd^{2+}, but also to the interfacial reduction reaction between Pd^{2+} and Ce^{3+}, reported after mixing Ce^{3+} precursor with Pd^{2+} and ammonia,[53] could contribute to the formation of Pd^0 particles.

Characterization of calcined coated foams

To obtain the final catalysts, deposited foams were calcined at 550 °C for 10 h. SEM images of the samples are shown in Fig. 2c-c2 and Fig. S1b-b3. During calcination the nitrates and water were removed, and an oxide scale developed (see below), consequently a ca. 5% weight loss occurred; however, some mechanical loss of the coating could not be discarded. Solid shrinking during weight loss and shearing stresses developed some more cracks in the layers. These phenomena were more important in compact coatings, leading to partial detachment in some localized regions. However, the calcination did not modify the morphology and size of the particles in the coating. Likewise, in electrodeposited samples, locally aggregated and well dispersed Pd-containing particles coexisted. For instance, even at the high resolution of FE-SEM (Fig. 2c2), although Pd signal was detected in the EDS spectra, there were not Pd particles identified.

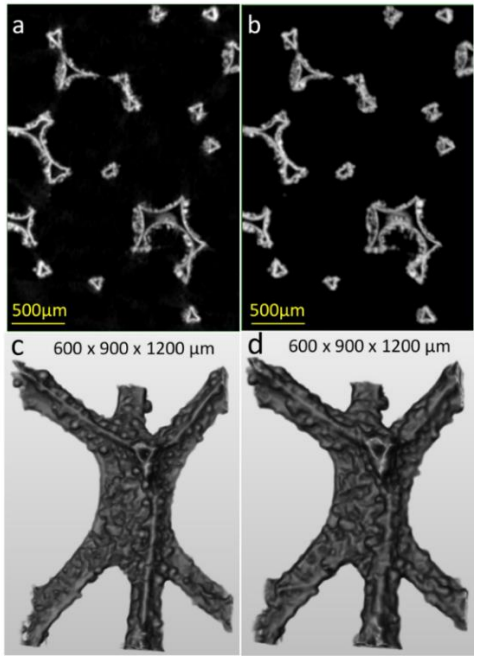

Fig. 5. Micro-computed tomography 2D slices and 3D reconstructions of 1200 µm foams before (a, c) and after coating with Pd-CeO_2 (b, d).

3D micro-computed tomography measurements of the whole foam disks before and after coating were recorded to have a larger samples overview (Fig. 5, Table 2). The presence of hollow struts with internal voids were clearly observed in Fig. 5a and 5b. From the solid structure thickness data (i.e. thickness of the hollow strut wall plus thickness of the coating), summarized in Table 2, a 5 µm average coating thickness was estimated, which is in the limit of the tomography resolution. The surface of the foam within the voids could also be coated by a thin layer, as identified in our previous work by a higher resolution nano-XRF/XRD tomography.[43] The coating layers only slightly reduced the total porosity of the foams and the mean pore sizes (values reported in Table 2 are actually an average of pore and cell sizes); rough surfaces and cellular structures were not largely altered. In Fig. 5d, it seemed that the coating was well-distributed in the triangular struts, and no accumulation in the valleys was observed. Thus, structured catalysts keep the low pressure drop and transport phenomena of the original bare foam.[54]

Table 2. Change in geometrical parameters of the foams before and after coating obtained by 3D micro-computed tomography measurements

Sample	Porosity* (%)	Mean pore size (µm)	Solid structure thickness (µm)
580 µm bare	89.3	511 ± 60	35 ± 8
580 µm coated	87.7	501 ± 59	41 ± 10
1200 µm bare	92.7	1058 ± 130	37 ± 11
1200 µm coated	91.1	1037 ± 136	42 ± 11

To further investigate the coatings at a higher magnification, HRTEM images of powders scratched away from the foam surfaces were collected (Fig. 6). CeO_2 nanoparticles with an ill-defined shape and average sizes of 5 – 15 and 3 – 10 nm were identified for CeO_2 and Pd-CeO_2, respectively (Fig. 6a, b). The combined analysis of HAADF images and EDS spectra again evidenced well dispersed palladium species (Fig. 6b3, b4, b5), there were no Pd-containing particles despite EDS Pd signal. They were related to Pd^{2+} inside the CeO_2 matrix in agreement with the signal at BE 337.9 eV in the Pd 3d core level in the XPS spectrum of the calcined (Fig. 4), which coexisted with Pd^0 (335.5 eV).

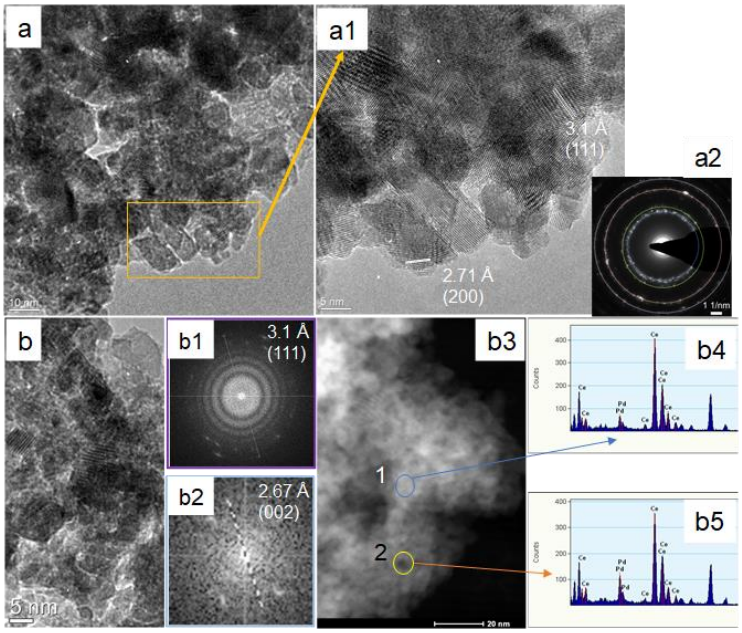

Fig. 6. Characterization of powders scratched from 580 µm coated foams. CeO_2: (a, a1) HRTEM images, (a2) SAED; Pd-CeO_2: (b) HRTEM images, (b1, b2) SAED, (b3) STEM-HAADF image, (b4, b5) EDS spectra from b3.

The presence of the solid solution may decrease the cubic fluorite sintering during calcination. Indeed, less crystalline nanoparticles (corresponding to more diffuse SAED diffraction rings) (Fig. 6a2, b1), and a broader F_{2g} mode in the Raman spectra (Fig. 2c3) were observed for Pd-CeO_2 than for CeO_2 samples after calcination. The specific surface areas of the Pd-CeO_2 calcined catalysts were 11.1 and 11.9 $m^2\ g^{-1}$, corresponding to 64.5 and 54.1 $m^2\ g^{-1}$ for the solid (Table 1). The increase in the surface area, in comparison to the fresh samples suggested the increase of the porosity, which might be related to the gases evolving during calcination. However, it should be considered that coating S_{BET} values may deviate from real ones since the catalytic loading could not be precisely obtained because of the modification of the metallic foam or loss of some coating as above commented. During calcination the foam was oxidized; in the Raman spectra of a calcined bare foam bands due to Fe_2O_3[55] or Fe^{3+} partially substituted by Al^{3+} in the Fe_2O_3 lattice[56] were recorded (Fig. S4).

The Raman spectra of calcined CeO_2 (Fig. 2c3) developed a small band at 250 cm^{-1} attributed to the normal Raman inactive (IR active) second-order transverse acoustic (2TA) mode,[57-59] which was previously reported in spectrum of electrodeposited CeO_2.[30] On the other hand, two new bands were registered at 196 and 651 cm^{-1} for Pd-CeO_2 (Fig. 2c3). The latter was attributed to the B_{1g} vibrational mode of square planar [PdO_4] subunits in the PdO structure,[60] which could be formed in regions of the coating with a high Pd/Ce ratio,[61] but that were not identified by XPS (PdO at BE ca. 336.9 eV).[62] The small peak at 196 cm^{-1} could also be related to the E_{u1} forbidden mode of PdO_4,[60] however, it was shifted from the 165 cm^{-1} value expected value in PdO, and its intensity did not follow the same trend than the B_{1g} mode. Hence, it was ascribed to PdO_4 in the ceria lattice as previously reported by Gualyev and co-workers.[40] It should be remarked that XRD patterns of the coated foams did not show any Pd^0 and PdO crystalline phase, suggesting either a low amount or poor crystallinity.

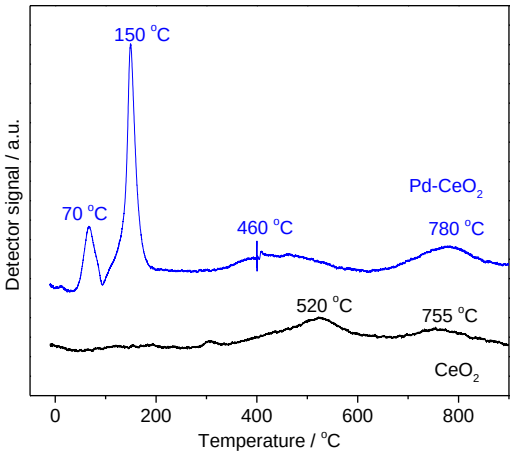

Fig. 7. H_2-TPR profiles of CeO_2 and Pd-CeO_2 coated on 580 µm foams.

The reducibility of coated foams during H_2-TPR profiles, shown in Fig. 7, was related to the above commented textural and structural features. The H_2 consumption profile of the CeO_2 showed the reduction steps of surface (520 °C) and bulk ceria (755 °C).[63] In Pd-CeO_2 sample, two peaks were recorded at ca 70 and 150 °C attributed to the reduction of PdO and well dispersed Pd-containing species interacting with the support, respectively.[32, 64-66] The reduction of CeO_2 could be overlapped in the second peak since palladium promoted its reduction; this promotion was also observed by the shift of the CeO_2 surface reduction towards lower temperatures and the decrease of the surface to bulk areas ratio. Despite Pd^0 particles were in the catalyst, the typical decomposition of palladium hydrides was not observed,[67] probably because of overlapped with the reduction peak of well dispersed Pd species and surface ceria in tight contact with Pd.

Catalytic activity in the CO oxidation

The samples coated by electrodeposition were finally tested in the CO oxidation reaction. As well documented in literature,[14] such a reaction shows significant activity even at low temperatures in presence of noble-metal catalysts, it does not produce intermediates and it is usually chosen as a model reaction for many environmental applications. Fig. 8 shows the CO ignition curves obtained with 1200 µm and 580 µm foams, respectively, changing the CO inlet concentration from 2% to 3%. From data collected on 1200 µm foam it is evident the effect of the CO concentration. The curve at 3% shows a higher light-off temperature, in agreement with literature studies that assume a negative reaction order of the CO;[68] this aspect is less evident on 580 µm foam. A second relevant aspect that can be noted for both samples is the null effect of the CO inlet concentration on the conversion at plateau, a typical feature of the physical regime.

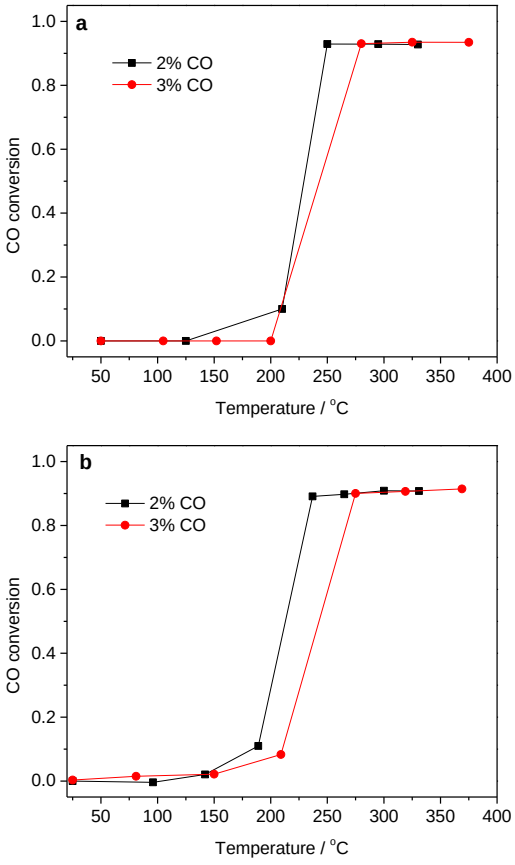

Fig. 8. CO ignition curves at 3 SLM tests in different CO concentrations for 580 µm foam (a) and for 1200 µm foam (b).

Fig. 9 shows the effect of the flow rate on the conversion at diffusive regime for both foams. In all the cases, significantly high CO conversions were obtained despite very low residence times (5.10^{-4} – 8.10^{-3} s). The very high geometrical surface of the foams enhances gas/solid interaction between the gas and the catalyst leading to very high volumetric mass transfer coefficients, calculated assuming an ideal plug flow reactor from the measured CO conversion as reported in Equation 1

$$k_v = k_c S_v = -\frac{\ln(1-\eta)\cdot Q}{V} \quad (1)$$

where k_v is the volumetric mass transfer coefficient [s^{-1}], k_c is the mass transfer coefficient [m s^{-1}], S_v is the geometric surface area [m^{-1}], η is the CO conversion, Q is the actual flow rate [m^3 s^{-1}] and V is the reactor volume [m^3].

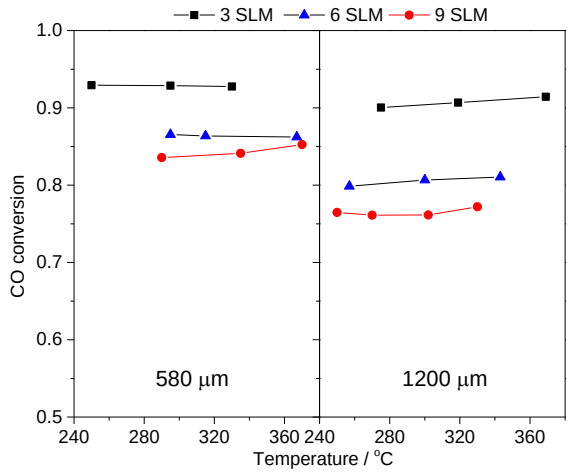

Fig. 9. Effect of the flow rate on the CO conversion over 580 µm foams and 1200 µm foams.

Calculated volumetric mass transfer coefficients for both foams are reported in Fig. 10. Values of volumetric mass transfer coefficients up to 1200 s^{-1} were measured in these conditions for 1200 µm foam and values up to 3600 s^{-1} for 580 µm foams, high cell density foams, which widely outperform state of the art 900 CPSI honeycombs, i.e k_v = 950 s^{-1} as calculated by Tronconi and Forzatti.[69] This aspect is central for the design of compact exhaust after-treatment systems where, due to the needs of more stringent environmental regulations, higher requirements on pollutant emissions will be necessary.

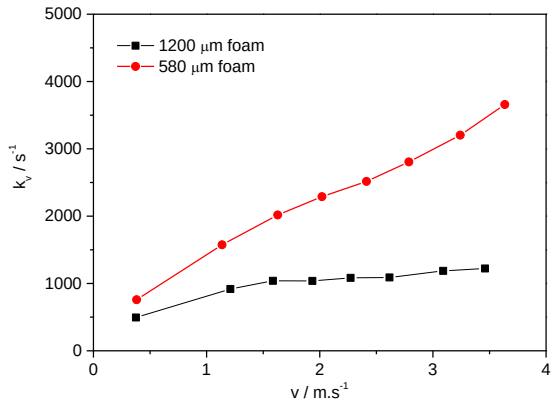

Fig. 10. Calculated volumetric mass transfer coefficients against actual flow velocity.

Tests at 3 SLM were repeated after some days of continuative operations of the rig in order to evaluate the stability of the coating under harsh conditions in terms of temperature gradients. In these specific conditions, both the number of thermal cycles and the hours of operation may influence the coating stability. Tests were performed after 24 h of operation and 6 thermal cycles and 48 h of operation and 12 thermal cycles for 1200 µm foam and only after and 48 h of operation after 12 thermal cycles for 580 µm foams. Results reported in Fig. 11 evidence that 1200 µm foams shows no decay of performances after 3 days and a decrease of just 1% of CO conversion after one week respect to the conversion curve obtained with fresh catalyst. 580 µm foam, instead, shows no decay of performances after one week suggesting a good quality and stability of the catalyst coating. Thus, the coating and Pd-containing species were characterized after the long-term catalytic tests.

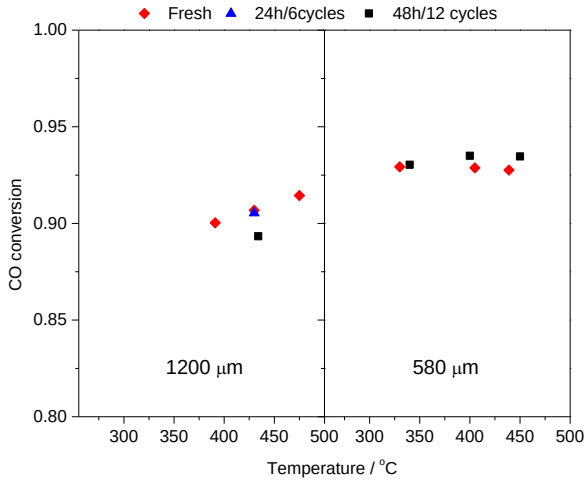

Fig. 11. Evaluation of the decay of performances of the catalyst over 1200 µm and 580 µm foams – diamonds: fresh catalyst, triangles: after 24 h and 6 thermal cycles, squares: after 48 h and 12 cycles.

Spent catalysts

In the characterization of the spent catalysts, special attention was paid to analyse different regions of the foam disks since axial temperature gradients generated during reaction conditions, i.e. 100-120 °C difference between the inlet and outlet of the bed.

The coating on the top of the foam disk, i.e. at the inlet of the catalytic bed, was less stable than the one at the bottom, being partially detached (Fig. 12a1, a2, Fig. S5). Conversely, the morphology of the CeO_2 particles was not modified at the inlet of the bed and well dispersed Pd species were found (Fig. 12a2). While the sintering of both the support and Pd occurred at the outlet, where spherical Pd particles, of around 25 nm were identified by FE-SEM (Fig. 12b2).

HRTEM images shown in Fig. 13 confirmed that the coating placed at the inlet of the bed was made by CeO_2 nanoparticles with dispersed Pd-containing species and Pd particles in the 2-7 nm range (4.1 ± 1.3 nm) (Fig. 13a-a2). On the other hand, both large CeO_2 (up to 100 nm) and Pd (14.9 ± 8.6 nm) particles were identified at the outlet of the bed, the latter being distributed both on the surface and in the bulk of ceria particles (Fig. 13b-b2). SAED analyses confirmed the presence of Pd^0 particles.

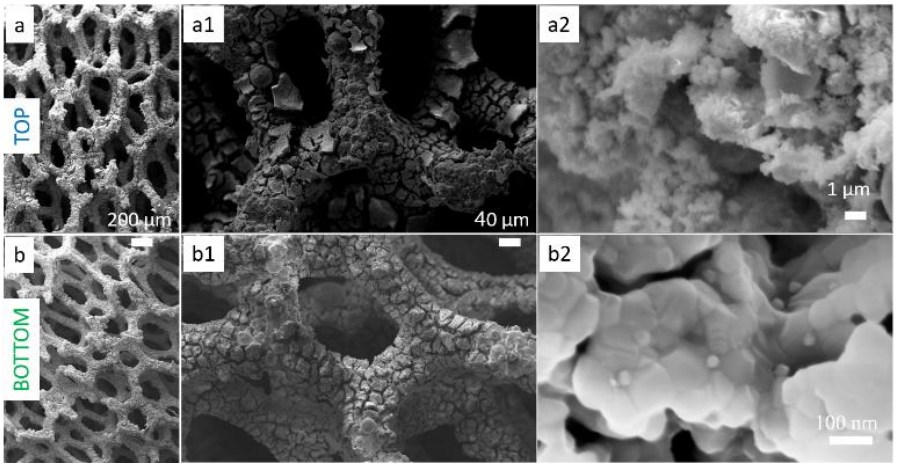

Fig. 12. SEM images of spent Pd-CeO_2 580 µmm foam catalyst: (a, a1, a2) top catalytic bed; (b, b1, b2) bottom catalytic bed, b2 is a FESEM image.

The modifications in the catalytic coating depending on the position in the bed were confirmed by XRD and Raman. Diffraction patterns in Fig. 14a and Raman spectra in Fig. 14b showed narrower CeO_2 reflections and F_{2g} modes, respectively, in spent than in calcined sample and in the bottom than in the top of the bed, due to ceria sintering. From SEM and HRTEM it would appear that the sintering did not modify the particle size at the top but it did at the bottom of the foam. Pd-containing species features also changed under reaction conditions. The Pd^0 (111) reflection, not observed in calcined catalysts, was recorded in the pattern of the spent catalysts, being more intense at the bottom of the bed. While in Raman spectra the band at 650 cm^{-1} due to PdO also become narrower at the outlet of the bed, but it was not visible at the inlet.

From these characterization results, it could be stated that the catalytic coating was rather stable in terms of adhesion, while CeO_2 sintered and Pd species were modified with time-on-stream due to the high flow rates, temperature and interaction with CO. In the fresh catalyst both Pd^0, PdO and Pd^{2+} in the solid solution were identified. Pd^0 is reported to have an increased activity in CO conversion[32, 33, 70, 71] and Pd^{2+} into CeO_2 generates oxygen vacancies responsible of activation of O_2.[72] Under reaction conditions, Pd^{2+} was reduced by CO to Pd^0 nanoparticles with a narrow size distribution at the inlet of the bed,[70, 72, 73] generating more active sites. At the outlet of the bed, the highest temperatures provoked the sintering of Pd^0 and PdO, which might be facilitated by the CeO_2 sintering. The coalescence of particles was observed in Fig. 13b, b1, however, the Ostwald ripening could also occur.[74] Furthermore, the less reducing atmosphere (lower CO concentration) decreased the reduction degree of the catalyst, indeed some PdO peaks were still observed in the Raman spectra. Thus, during the CO oxidation test, the active sites were modified by simultaneous transformations, namely generation of new Pd^0 sites and their loss due to the partial sintering, this behaviour, together with the fact that tests were performed under diffusive controlled regime, may explain the absence of differences in the activity with the number of cycles.

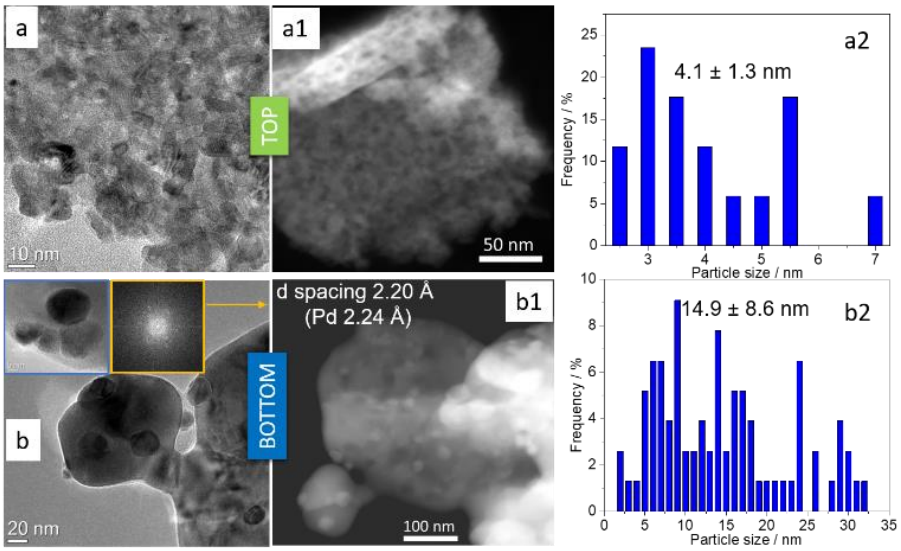

Fig. 13. HRTEM characterization of spent Pd-CeO_2 on 580 µm foam catalyst. Top: (a) HRTEM, (a1) STEM-HAADF; (a2) particle size distribution. Bottom: (b) HRTEM, (b1) STEM-HAADF, (b2) particle size distribution. Insets of Figure b: high magnification image of Pd particles (left) and FFT (right).

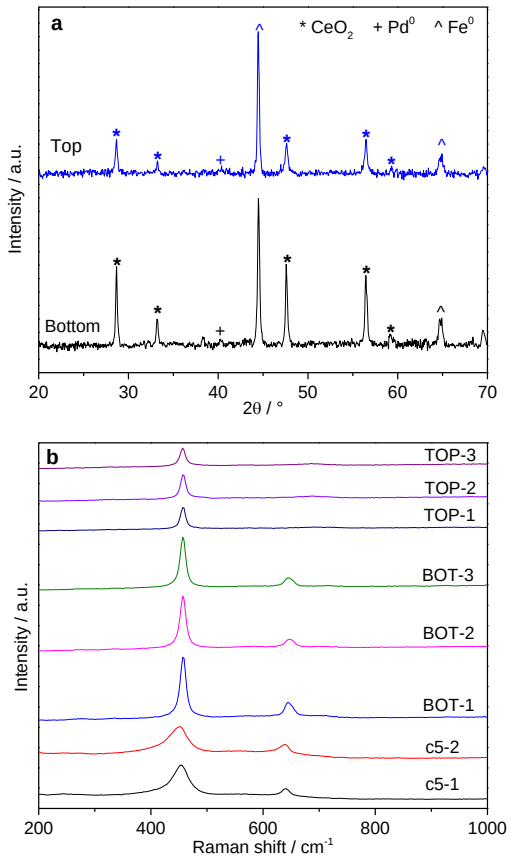

Fig. 14. XRD patterns (a) and Raman spectra (b) of spent Pd-CeO_2 580 µm foam catalyst.

Conclusions

This study demonstrated that the electrodeposition is a promising one-step method to coat high pore density open-cell foams with active and stable Pd-CeO_2 catalysts for mass transfer controlled reactions, such as CO oxidation and many other environmental catalytic processes.

A cubic fluorite nano-CeO_2 with defects was homogeneously deposited on the foam surface by the electro-base generation method forming a coating with vertically oriented platelets and compact particles; the process being independent on the pore size. During the synthesis procedure, Pd^{2+} was incorporated into CeO_2 forming a $Pd_xCe_{1-x}O_{2-\delta}$ solid solution. The massive Pd^{2+} to Pd^0 reduction did not occur, but the formation of Pd^0 particles could not be completely avoided because the direct electrochemical reduction or interfacial reduction reaction between Pd^{2+} and Ce^{3+}, which was also observed in conventional coprecipitation.

The porous coating with perpendicularly orientated particles may better withstand shrinking and shearing stresses than compact layers enhancing the stability during calcination and reaction conditions. While the conservation of the solid $Pd_xCe_{1-x}O_{2-\delta}$ solution may help to decrease the CeO_2 sintering. These highly dispersed Pd^{2+} species in the solid solution generated small Pd^0 nanoparticles that were also stable against sintering at the inlet of the bed, 4.1 ± 1.3 nm, but sensible to coalescence or Ostwald ripening when high temperatures were reached at the outlet.

The stable coating with dispersed Pd species all over the foam surface provided both high activities and stabilities in the CO oxidation operating at very high GHSV. While the very high geometrical specific surface of the foams enhanced gas/solid interaction leading to volumetric mass transfer coefficients larger than their honeycomb state of the art counterparts. Consequently, electrodeposited Pd-CeO_2 catalysts are promising for compact exhaust after-treatment systems.

Conflicts of interest

There are no conflicts to declare.

Acknowledgements

P.H. Ho thanks to SINCHEM grant for Ph.D. research fellowship. SINCHEM is a joint-doctorate programme selected under Erasmus Mundus Action 1 programme (FBA 2013-0037).

Notes and references

1 T. Montini, M. Melchionna, M. Monai, P. Fornasiero, *Chem. Rev.*, 2016, **116**, 5987–6041.
2 J. W. Kim, B. K. Choi, M. J. Jang, Patent US 20170210090 A1, (2017).
3 P. Fornasiero, T. Montini, M. Graziani, S. Zilio, M. Succi, *Catal. Today*, 2008, **137**, 475–482.
4 E. Tronconi, G. Groppi, C. G. Visconti, *Curr. Opin. Chem. Eng.*, 2014, **5**, 55–67.
5 S. Colussi, A. Gayen, M. Farnesi Camellone, M. Boaro, J. Llorca, S. Fabris, A. Trovarelli, *Angew. Chem. Int. Ed.*, 2009, **48**, 8481–8484.
6 S. Colussi, A. Trovarelli, E. Vesselli, A. Baraldi, G. Comelli, G. Groppi, J. Llorca, *Appl. Catal. A: Gen.*, 2010, **390**, 1–10.
7 A. D. Mayernick, M. J. Janik, *J. Catal.*, 2011, **278**, 16–25.
8 M. Cargnello, J. J. D. Jaén, J. C. H. Garrido, K. Bakhmutsky, T. Montini, J. J. C. Gámez, R. J. Gorte, P. Fornasiero, *Science*, 2012, **337**, 713–717.
9 R. J. Gorte, *AIChE J.*, 2010, **56**, 1126–1135.
10 S. Hilaire, X. Wang, T. Luo, R. J. Gorte, J. Wagner, *Appl. Catal. A: Gen.*, 2001, **215**, 271–278.
11 M. Cargnello, T. Montini, S. Polizzi, N. L. Wieder, R. J. Gorte, M. Graziani, P. Fornasiero, *Dalton Trans.*, 2010, **39**, 2122–2127.
12 Q. Zhang, Y. Li, R. Chai, G. Zhao, Y. Liu, Y. Lu, *Appl. Catal. B: Env.*, 2016, **187**, 238–248.
13 V. Palma, D. Pisano, M. Martino, *Int. J. Hydrogen Energy*, 2017, **42**, 23517–23525.
14 L. Giani, G. Groppi, E. Tronconi, *Ind. Eng. Chem. Res.*, 2005, **44**, 4993–5002.
15 G. Incera Garrido, F. C. Patcas, S. Lang, B. Kraushaar-Czarnetzki, *Chem. Eng. Sci.*, 2008, **63**, 5202–5217.
16 P. Aghaei, C. G. Visconti, G. Groppi, E. Tronconi, *Chem. Eng. J.*, 2017, **321**, 432–446.
17 A. Montebelli, C. G. Visconti, G. Groppi, E. Tronconi, S. Kohler, H. J. Venvik, R. Myrstad, *Appl. Catal. A: Gen.*, 2014, **481**, 96–103.

18 M. Frey, T. Romero, A. C. Roger, D. Edouard, *Catal. Today*, 2016, **273**, 83–90.
19 F. J. Méndez, O. Sanz, M. Montes, J. Guerra, C. Olivera-Fuentes, S. Curbelo, J. L. Brito, *Catal, Today*, 2017, **289**, 151–161.
20 P. S. Roy, C. S. Park, A. S. K. Raju, K. Kim, *J. CO_2 Util.*, 2015, **12**, 12–20.
21 Q. Zhang, Y. Li, R. Chai, G. Zhao, Y. Liu, Y. Lu, *Appl. Catal. B: Env.*, 2016, **187**, 238–248.
22 R. Chai, Z. Zhang, P. Chen, G. Zhao, Y. Liu, Y. Lu, *Micropor. Mesopor. Mater.*, 2017, **253**, 123–128.
23 P. Benito, W. De Nolf, G. Nuyts, M. Monti, G. Fornasari, F. Basile, K. Janssens, F. Ospitali, E. Scavetta, D. Tonelli, A. Vaccari, *ACS Catal.*, 2014, **4**, 3779–3790.
24 P. Benito, G. Nuyts, M. Monti, W. De Nolf, G. Fornasari, K. Janssens, E. Scavetta, A. Vaccari, *Appl. Catal. B: Environ.*, 2015, **179**, 321–332.
25 J. A. Switzer, *Am. Ceram. Soc. Bull.*, 1987, **66**, 1521–1525.
26 I. Zhitomirsky, A. Petric, *Mater. Lett.*, 1999, **40**, 263–268.
27 L. Arurault, P. Monsang, J. Salley, R. S. Bes, *Thin Solid Films*, 2004, **466**, 75–80.
28 Y. Hamlaoui, F. Pedraza, C. Remazeilles, S. Cohendoz, C. Rébéré, L. Tifouti, J. Creus, *Mater. Chem. Phys.*, 2009, **113**, 650–657.
29 L. Yang, X. Pang, G. Fox-Rabinovich, S. Veldhuis, I. Zhitomirsky, *Surf. Coat. Technol.*, 2011, **206**, 1–7.
30 P. Bocchetta, M. Santamaria, F. Di Quarto, *J. Appl. Electrochem.*, 2009, **39**, 2073–2081.
31 L. Giani, C. Cristiani, G. Groppi, E. Tronconi, *Appl. Catal. B: Env.*, 2006, **62**, 121–131.
32 M. Kurnatowska, L. Kepinski, W. Mista, *Appl. Catal. B*, 2012, **117–118**, 135–147.
33 A. I. Boronin, E. M. Slavinskaya, I. G. Danilova, R. V. Gulyaev, Yu. I. Amosov, P. A. Kuznetsov, I. A. Polukhina, S. V. Koscheev, V. I. Zaikovskii, A. S. Noskov, *Catal. Today*, 2009, **144**, 201–211.
34 G. Glaspell, L. Fuoco, M. Samy El-Shall, *J. Phys. Chem. B*, 2005, **109**, 17350–17355.
35 G. Li, L. Li, D. Jiang, Y. Li, J. Shi, *Nanoscale*, 2015, **7**, 5691–5698.
36 K. R. Priolkar, P. Bera, P. R. Sarode, M. S. Hegde, S. Emura, R. Kumashiro, N. P. Lalla, *Chem. Mater.*, 2002, **14**, 2120–2128.
37 M. Cargnello, V. V. T. Doan-Nguyen, T. R. Gordon, R. E. Diaz, E. A. Stach, R. J. Gorte, P. Fornasiero, C. B. Murray, *Science*, 2013, 341, 771–773.
38 H. Liang, J. M. Raitano, G. He, A. J. Akey, I. P. Herman, L. Zhang, S. W. Chan, *J. Mater. Sci.*, 2012, **47**, 299–307.
39 E. M. Slavinskaya, R. V. Gulyaev, A. V. Zadesenets, O. A. Stonkusa, V. I. Zaikovskiia, Yu. V. Shubin, S. V. Korenev, A. I. Boronin, *Appl. Catal. B: Env.*, 2015, **166–167**, 91–103.
40 R. V. Gulyaev, T. Yu. Kardash, S. E. Malykhin, O. A. Stonkus, A. S. Ivanova, A. I. Boronin, *Phys. Chem. Chem. Phys.*, 2014, **16**, 13523–13539.
41 G. Li, L. Li, D. Jiang, *J. Phys. Chem. C*, 2015, **119**, 12502−12507.
42 E. Verlato, S. Barison, S. Cimino, L. Lisi, G. Mancino, M. Musiani, F. Paolucci, *Chem. Eng. J.*, 2017, **317**, 551–560.
43 P. H. Ho, W. de Nolf, F. Ospitali, A. Gondolini, G. Fornasari, E. Scavetta, D. Tonelli, A. Vaccari, P. Benito, *Appl. Catal. A: Gen.*, 2018, **560**, 12–20.
44 T. Hildebrand, P. Ruegsegger, *J Microsc-Oxford*, 1997, **185**, 67–75.
45 B. Bouchaud, J. Balmain, G. Bonnet, F. Pedraza, *Appl. Surf. Sci.*, **268**, 218–224.
46 L. Arurault, B. Daffos, F. X. Sauvage, *Mater. Res. Bull.*, 2008, **43**, 796–805.
47 Y. Hamlaoui, C. Rémazeilles, M. Bordes, L. Tifouti, F. Pedraza, *Corros. Sci.*, 2010, **52**, 1020–1025.
48 M. Thommes, K. Kaneko, A. V. Neimark, J. P. Olivier, F. Rodriguez-Reinoso, J. Rouquerol, K. S. W. Sing, *Pure Appl. Chem.*, 2015, **87**, 1051–1069.
49 S. Hinokuma, H. Fujii, M. Okamoto, K. Ikeue, M. Machida, *Chem. Mater.*, 2010, **22**, 6183–6190.
50 A. I. Boronin, E. M. Slavinskaya, I. G. Danilova, R. V. Gulyaev, Y. I. Amosov, P. A. Kuznetsov, I. A. Polukhina, S. V. Koscheev, V. I. Zaikovskii, A. S. Noskov, *Catal. Today*, 2009, **144**, 201–211.
51 J. M. Gatica, R. T. Baker, P. Fornasiero, S. Bernal, G. Blanco, J. Kaspar, *J. Phys. Chem. B*, 2000, **104**, 4667–4672.
52 J. A. Abys, Palladium Electroplating in Modern Electroplating, 5th Edition, (M. Schlesinger, M. Paunovic, eds.), Willey, 2011.
53 X. Wang, D. Liu, J. Li, J. Zhen, F. Wang, H. Zhang, *Chem. Sci.*, 2015, **6**, 2877–2884.
54 M. Bracconi, M. Ambrosetti, M. Maestri, G. Groppi, E. Tronconi, *Chem. Eng. J.*, 2017, **315**, 608–620.
55 D. L. A. de Faria, S. Venâncio Silva, M. T. de Oliveira, *J. Raman Spectrosc.*, 1997, **28**, 873–878.
56 A. Zoppi, C. Lofrumento, E. M. Castellucci, Ph. Sciau, *J. Raman Spectrosc.*, 2008, **39**, 40–46.
57 W. H. Weber, K. C. Bass, J. R. McBride, *Phys. Rev. B*, 1993, **48**, 178–185.
58 B. M. Reddy, A. Kahn, Y. Yamada, T. Kobayashi, S. Loridant, J. C. Volta, *J. Phys. Chem. B*, 2003, **107**, 5162–5167.
59 Z. Hu, X. Liu, D. Meng, Y. Guo, Y. Guo, G. Lu, *ACS Catal.*, 2016, **6**, 2265−2279.
60 J. R. McBride, K. C. Hass, W. H. Weber, *Phys. Rev. B*, 1991, **44**, 5016–5028.
61 C. I. Hiley, J. M. Fisher, D. Thompsett, R. J. Kashtiban, J. Sloan, R. I. Walton, *J. Mater. Chem. A*, 2015, **3**, 13072–13079.
62 E. Vilarrasa-García, A. Infantes-Molina, R. Moreno Tost, E. Rodríguez-Castellón, A. Jiménez-López, C. L. Cavalcante Jr, D. C. S. Azevedo, *Energy Fuels*, 2010, **24**, 3436–3442.
63 F. Giordano, A. Trovarelli, C. de Leitenburg, M. Giona, *J. Catal.*, 2000, **193**, 273–282.
64 L. Meng, J. J. Lin, Z. Y. Pu, L. F. Luo, A. P. Jia, W. X. Huang, M. F. Luo, J. Q. Lu, *Appl. Catal. B: Env.*, 2012, **119–120**, 117–122.
65 H. Zhu, Z. Qin, W. Shan, W. Shen, J. Wang, *J. Catal.*, 2004, **225**, 267–277.
66 Y. Luo, Y. Xiao, G. Cai, Y. Zheng, K. Wei, *Appl. Catal. B: Env.*, 2013, **136–137**, 317–324.
67 C. B. Wang, H. K. Lin, C. M. Ho, *J. Molec. Catal. A: Chem.*, 2002, **180**, 285–291.
68 E. Tronconi, G. Groppi, *Chem. Eng. Sci.*, 2000, **55**, 6021–6036.
69 E. Tronconi, P. Forzatti, *AIChE J.*, 1992, **38**, 201–210.
70 M. Fernández-García, A. Martínez-Arias, L. N. Salamanca, J. M. Coronado, J. A. Anderson, J. C. Conesa, J. Soria, *J. Catal.*, 1999, **187**, 474−485.
71 S. Hinokuma, H. Fujii, Y. Katsuhara, K. Ikeuea, M. Machida, *Catal. Sci. Technol.*, 2014, **4**, 2990–2996.
72 L. Meng, A. P. Jia, J. Q. Lu, L. F. Luo, W. X. Huang, M. F. Luo, *J. Phys. Chem. C*, 2011, **115**, 19789–19796.
73 E. Sasmaz, C. Wang, M. J. Lance, J. Lauterbach, *J. Mater. Chem. A*, 2017, **5**, 12998–13008.
74 Y. Q. Su, J. X. Liu, I. A. W. Filot, E. J. M. Hensen, *Chem. Mater.*, 2017, **29**, 9456−9462.